INTERNATIONAL JOURNAL FOR NUMERICAL METHODS IN FLUIDS
Int. J. Numer. Meth. Fluids 2002; **40**:953–980 (DOI: 10.1002/fld.395)

Computational predictability of time-dependent natural convection flows in enclosures (including a benchmark solution)

Mark A. Christon[1,*,†], Philip M. Gresho[2] and Steven B. Sutton[3]

[1]*Sandia National Laboratories M/S 0819, P.O. Box 5800, Albuquerque, NM 87185-0819, U.S.A.*
[2]*Lawrence Livermore National Laboratory (retired), L-103, P.O. Box 808, Livermore, CA 94550, U.S.A.*
[3]*Lawrence Livermore National Laboratory, L-463, P.O. Box 808, Livermore, CA 94450, U.S.A.*

SUMMARY

This paper summarizes the results from a special session dedicated to understanding the fluid dynamics of the 8:1 thermally driven cavity which was held at the First MIT Conference on Computational Fluid and Solid Dynamics in June, 2001. The primary objectives for the special session were to: (1) determine the most accurate estimate of the critical Rayleigh number above which the flow is unsteady, (2) identify the correct, i.e. best time-dependent benchmark solution for the 8:1 differentially heated cavity at particular values of the Rayleigh and Prandtl numbers, and (3) identify those methods that can reliably provide these results. Copyright © 2002 John Wiley & Sons, Ltd.

KEY WORDS: 8:1 thermally driven cavity; CFD; Boussinesq equations; incompressible flow

1. INTRODUCTION AND BACKGROUND

Modern thermal design practices often rely on a 'predictive' simulation capability—although predictability is rarely quantified and often difficult to confidently achieve in practice. Nevertheless, the computational predictability of laminar natural convection in enclosures is a significant issue for many industrial thermal design problems. One example of this is the design-for-mitigation of optical distortion due to buoyancy-driven flow in large-scale laser systems.

In many instances the sensitivity of buoyancy-driven enclosure flows can be linked to the presence of multiple bifurcation points that yield laminar thermal convective processes which can transit from steady to various modes of unsteady flow [1]. This behaviour is brought to light by a problem as 'simple' as a differentially heated tall rectangular cavity (8:1 height/width aspect ratio) filled with a Boussinesq fluid with $Pr = 0.71$—which partially defines the focus of

* Correspondence to: M. A. Christon, Computational Physics R & D Department, Sandia National Laboratories, M/S 0819, P.O. Box 5800, Albuquerque, New Mexico 87185-0819, U.S.A.
† E-mail: machris@sandia.gov

Received 31 December 2001
Revised 1 July 2002

this work. For our purposes, the differentially heated cavity provides a virtual fluid dynamics laboratory as pointed out by Le Quéré [2]:

> 'In conclusion let us emphasize that the differentially heated cavity, in addition to its relevance as a model of convective heat transfer, turns out to be a real fluid mechanics laboratory in itself. The spatial structure of the flow is made of vertical and horizontal boundary layers, of corner structures, of a stratified core... which depend very sensitively on the aspect ratio, Prandtl number and thermal boundary conditions (even a fly-wheel structure can be found at low Pr). All these features co-operate to give rise to very complex time behaviours resulting from several instability mechanisms, travelling waves in the vertical boundary layers, thermal instabilities along the horizontal walls in particular, which can interact strongly with internal wave dynamics.'

The flow fields, and associated eigenmodes, in the 8:1 cavity exhibit two types of symmetry that are central to understanding the overall behaviour of the enclosure flow and its associated stability with respect to the three primary problem parameters, Rayleigh number Ra, Prandtl number Pr and cavity aspect ratio A. For the 8:1 differentially heated cavity with $0 \leqslant x \leqslant W$, $0 \leqslant y \leqslant H$, centre at $(x, y) = (W/2, H/2)$, and vertical walls with prescribed temperatures at $\theta(0, y) = \frac{1}{2}$ and $\theta(W, y) = -\frac{1}{2}$, the Boussinesq form of the incompressible Navier–Stokes equations admit solutions with the so-called centro-symmetry property—see Reference [3], or more recently, Reference [4].

The centro-symmetry property consists of cyclic-symmetry of order 2 about the cavity centre in the primary flow fields where cyclic-symmetry is defined by a single rotation through an angle $\zeta = 2\pi/n$ with n defining the order of the cyclic-symmetry. The cyclic-symmetry ($\zeta = \pi$) inherent in the observed centro-symmetry for the 8:1 cavity consists of 'skew-symmetry' in the velocity and non-dimensional temperature, and 'symmetry' in the pressure field, i.e.

$$\begin{aligned} u(W - x, H - y) &= -u(x, y) \\ v(W - x, H - y) &= -v(x, y) \end{aligned} \tag{1}$$

$$\begin{aligned} \theta(W - x, H - y) &= -\theta(x, y) \\ P(W - x, H - y) &= P(x, y) \end{aligned} \tag{2}$$

where the hydrostatic part of the pressure, P, is assumed to be zero at the cavity centre. In both cases, this is a cyclic-symmetry of order 2. Here, and throughout this journal issue dedicated to the 8:1 cavity, 'skew-symmetry' for the differentially heated cavity is used to indicate that there is skew-symmetry in the velocity components and non-dimensional temperature. The centro-symmetry property implies a concomitant symmetry in the pressure. Again, all symmetries are with respect to the centre of the cavity. In the cavity problem in this and the other papers in this special issue, it is worth noting that the temperature boundary conditions are skew-symmetric.

The eigenmodes for the differentially heated cavity may either share the centro-symmetry property or have the 'opposite' symmetry wherein the velocity and scaled temperature are symmetric but the pressure field is skew-symmetric with respect to the cavity centre (see Reference [4]). In this case, the flow fields still exhibit cyclic-symmetry of order 2 about the

cavity centre. Eigenmodes that exhibit symmetry in the velocity and scaled temperature with skew-symmetry in the pressure field are referred to as 'centro-symmetry-breaking' or simply 'symmetry-breaking' eigenmodes.

In the 8:1 cavity, the spectrum of the Jacobian of the Navier–Stokes equations about a steady-state solution is characterized by an infinite number of eigenvalues which are either real or occur in complex conjugate pairs. For increasing Rayleigh number (Ra), some of the eigenvalue pairs cross the imaginary axis indicating bifurcation points (i.e. steady flow becomes unsteady, á la Hopf). Preliminary computations in the air-filled 8:1 cavity (Xin and Le Quéré [5]) indicated that two pairs of complex conjugate eigenvalues cross the imaginary axis in the vicinity of $Ra = 3.1 \times 10^5$. One of the corresponding eigenmodes shares the centro-symmetry property of the base flow, while the other, the first unstable mode, in fact, does not.

The presence of two types of unstable eigenmodes suggests that there may be significant sensitivity to the choice of initial conditions. That is, the choice of skew-symmetric conditions may promote the saturation of the second unstable mode which exhibits skew-symmetry in the velocities and non-dimensional temperature. In contrast, a random perturbation of the temperature field around the mean may promote the growth of the first unstable mode, i.e. the symmetry-breaking mode, at least for a finite period of time. Due, in part, to the presence of multiple unstable modes with a relatively small separation in Ra, the ostensibly simple differentially heated cavity problem is not as simple as one might initially believe.

Additionally, the simulation of this buoyancy-driven flow is remarkably susceptible to the deleterious effects of numerical damping and/or dispersion introduced by commonly used CFD 'tricks-of-the-trade', thus making it surprisingly challenging. For example, preliminary numerical tests demonstrated that the damping/dispersion artifacts from the simplest time-marching advection treatment with an added balancing tensor diffusivity (see for example, Reference [6]) can destroy the delicate thermal convective processes present in this enclosure when close to the critical Rayleigh number. In fact, coarse-grid computations can exhibit steady-state solutions even though the true solution is unsteady—requiring higher resolution grids than may be initially thought. For another example, the very instability under investigation turns out to be a boundary layer instability *in the flow direction*, thus rendering suspicious any additional streamline upwinding—*ad hoc* or otherwise. Even when dissipation and dispersion have seemingly been minimized, computational experiments have shown that the amplitude of the periodic temperature oscillations can vary by as much as an order of magnitude depending on the specifics of the spatial discretization, grid resolution, stopping criteria for iterative solvers, and even the use of advective vs conservative forms of the governing equations.

Ultimately the sensitivity of this class of flow problem to initial and boundary conditions, formulation details, and numerical procedures raises at least the following questions: What is the critical Rayleigh number, above which the flow will be unsteady, for the 8:1 enclosure? What is the behaviour of the flow field at Rayleigh numbers slightly above critical? What is the role of linear stability analyses in predicting unstable modes? Can non-linear dynamics provide any insight into the behaviour of the 8:1 cavity? What can be said about the relationship between (unstable) steady-state solutions and time-averaged periodic solutions? What is the best formulation and associated numerical procedure to use in order to ameliorate the sensitivities observed in practice and raise the level of accurate predictability? Which 'other' numerical methods, i.e. discretization, time integrator, stabilization, preconditioned iterative technique and 'tricks of the trade' are at least viable—and which are not?

In an attempt to answer these questions, a special session was organized for the First MIT Conference on Computational Fluid and Solid Mechanics [7]. The session organizers solicited contributed solutions to the 8:1 differentially-heated cavity problem for near-critical Rayleigh numbers with the goal of attracting practitioners of finite difference, finite volume, finite element and spectral methods to this seemingly simple 2-D problem. The application of commercial CFD codes was also highly encouraged—and still is.

In the subsequent sections of this paper, the problem definition for the 8:1 differentially heated cavity is presented along with a summary of the compulsory data requested by the session organizers. Following the problem definition is an overview of the solution methods that were applied to the 8:1 cavity problem and their corresponding contributed solutions. Finally, the contributed compulsory data is compared using a series of metrics to indicate the overall accuracy and performance of the methods and codes applied to the 8:1 cavity.

2. PROBLEM DEFINITION

The buoyancy driven enclosure flow problem is based upon the geometry shown in Figure 1 where W is the width and H the height of the enclosure. The enclosure aspect ratio is $A=H/W$ and takes on the value $A=8$. The gravity vector is directed in the negative

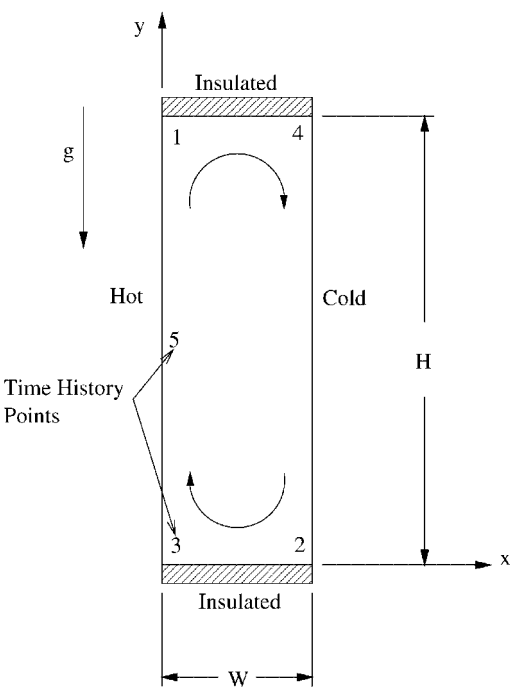

Figure 1. Differentially heated enclosure with 8:1 aspect ratio (not to scale), insulated horizontal walls and constant temperature vertical walls.

y-coordinate direction, and the Boussinesq approximation is assumed to be valid, i.e. only small temperature excursions from the mean temperature are admitted.

The non-dimensional governing equations for the time-dependent thermal convection problem are the incompressible Navier–Stokes equations, conservation of mass and the energy equation written here in terms of temperature:

$$\frac{\partial \mathbf{u}}{\partial t} + \mathbf{u} \cdot \nabla \mathbf{u} = -\nabla P + \sqrt{\frac{Pr}{Ra}} \nabla^2 \mathbf{u} + \hat{j}\theta \tag{3}$$

$$\nabla \cdot \mathbf{u} = 0 \tag{4}$$

and

$$\frac{\partial \theta}{\partial t} + \mathbf{u} \cdot \nabla \theta = \frac{1}{\sqrt{Ra\,Pr}} \nabla^2 \theta \tag{5}$$

where, $\mathbf{u} = (u, v)$, P and θ are the velocity, the deviation from hydrostatic pressure, and temperature, respectively, and $\hat{j}$ is the unit vector in the y direction. These non-dimensional equations were obtained using the characteristic length W, buoyancy velocity scale $U = \sqrt{g\beta W \Delta T}$, time scale $\tau = W/U$ and pressure $\tilde{P} = \rho U^2$. Here, ρ is the mass density, g the gravitational acceleration, and β the coefficient of thermal expansion. The non-dimensional temperature is defined in terms of the wall temperature difference and a reference temperature as

$$\theta = \frac{T - T_r}{T_h - T_c} \tag{6}$$

where

$$T_r = \frac{T_h + T_c}{2} \tag{7}$$

and T_h is the prescribed temperature of the hot wall, and T_c is that of the cold wall.

The Rayleigh number is

$$Ra = \frac{g\beta \Delta T W^3}{v\alpha} \tag{8}$$

and the Prandtl number is

$$Pr = v/\alpha \tag{9}$$

where α is the thermal diffusivity, v the kinematic viscosity, and $\Delta T = T_h - T_c$ the temperature difference between the hot and cold walls. For all contributed calculations we requested that $Pr = 0.71$, and $Ra = 3.4 \times 10^5$. Additional information relevant to this problem may be found in References [2, 8–10].

2.1. Boundary conditions

The enclosure boundary conditions are simple and consist of no-slip and no-penetration walls, i.e. $u = v = 0$ on all four walls. The thermal boundary conditions on the left and right walls are

$$\begin{aligned} \theta|_{x=0} &= +\tfrac{1}{2} \\ \theta|_{x=W} &= -\tfrac{1}{2} \end{aligned} \tag{10}$$

and along the bottom and top walls,

$$\left.\frac{\partial\theta}{\partial y}\right|_{y=0}=0$$
$$\left.\frac{\partial\theta}{\partial y}\right|_{y=H}=0 \tag{11}$$

2.2. Initial conditions

One set of initial conditions that may be used for a transient simulation consist of an isothermal fluid initially at rest, i.e.

$$\mathbf{u}(\mathbf{x},0)=0 \tag{12}$$

and

$$\theta(\mathbf{x},0)=0 \tag{13}$$

which are compatible with the skew-symmetric solution.

In the original call for contributed solutions, the use of alternative initial conditions was encouraged as a means to test the sensitivity of the problem to them. For example, a random perturbation of the initial constant temperature was also an acceptable initial condition—as were any others that were not skew-symmetric.

3. COMPULSORY AND OPTIONAL RESULTS

This section outlines the quantities of primary interest that were considered compulsory for the benchmark problem, and suggests some additional quantities that were not required, but that contributors were encouraged to report. The compulsory results for the special session were to be presented in three tables containing point, wall, and global time history and time-averaged data, and two plots showing the temperature time history and a skewness metric to be defined later. For the MIT special session, we encouraged the submission of results from steady state, transient, and stability computations and the use of both research and commercial flow solvers.

The compulsory results for the benchmark problem were to be prepared for $Pr=0.71$ and $Ra=3.4\times10^5$. There was no restriction on the submission of results for additional Rayleigh numbers and we encouraged participants to include their best prediction of the critical Rayleigh number, Ra_{crit}, which marks the transition from steady to time-periodic behaviour. The initial call for contributed solutions gave our estimate of the critical Rayleigh number at that time which we believed to be $Ra_{\text{crit}}\approx3.1\times10^5$.

The compulsory data for the transient and steady-state computations were categorized according to the data type, i.e. point, wall and global data. For all time-dependent computations, the average value and the peak-to-valley oscillation amplitude were to be tabulated, along with the period of oscillation for all compulsory data.

The computation of an average value was based upon achieving a statistically stationary state where the period and amplitude were essentially constant. For a generic variable, ϕ,

Table I. Non-dimensional co-ordinates of time-history points.

Point	x-Co-ordinate	y-Co-ordinate
1	0.1810	7.3700
2	0.8190	0.6300
3	0.1810	0.6300
4	0.8190	7.3700
5	0.1810	4.0000

e.g. $\phi = u, v, \theta, \ldots$, the average was to be computed as

$$\bar{\phi} = \frac{1}{T} \int_t^{t+T} \phi(\mathbf{x}, t)\, \mathrm{d}t \tag{14}$$

where T represents the period of time for which the average was computed. The oscillatory component was to be computed as

$$\phi'(\mathbf{x}, t) = \phi(\mathbf{x}, t) - \bar{\phi} \tag{15}$$

The average was requested for one or more complete periods where the amplitude and period were essentially constant, i.e. after the startup transients completed. Note that for non-linear oscillations, the mean amplitude is generally different from the average of the peak and valley extrema.

3.1. Grid resolution guidelines

There were no strict requirements on grid resolution, however, all participants were asked to provide results that they believed to be sufficiently accurate. For the purposes of grid generation, contributors were directed to Reference [3] for guidance on the vertical-wall boundary layer thickness. We suggested using graded meshes with approximately a 1:5 x-to-y ratio of grid points starting with a coarse grid of 21×101 and increasing the grid resolution by grid doubling, e.g. a medium grid of 41×201 and a fine grid of 81×401. Uniform meshes will, of course, require more nodes.

3.2. Point data

Time-history data was requested at the time-history points shown in Figure 1 and identified in Table I. The compulsory point data consisted of velocity (u, v), temperature θ, stream function ψ, and vorticity ω at time-history point-1. A plot of the oscillatory variation in temperature at point-1, θ_1, was to accompany the tabulated results.

For our purposes, the vorticity was defined as

$$\omega = \frac{\partial v}{\partial x} - \frac{\partial u}{\partial y} \tag{16}$$

and the stream function as

$$u = \frac{\partial \psi}{\partial y}, \quad v = -\frac{\partial \psi}{\partial x} \tag{17}$$

with $\psi = 0$ on the walls.

As a part of the compulsory data, we also requested that a skewness metric, ε_{12}, for the temperature field be reported. The skewness metric was defined using time-history points 1 and 2 as

$$\varepsilon_{12} = \theta_1 + \theta_2 \tag{18}$$

and provided a measure of the loss of skew-symmetry in the temperature field. For flow solutions with the centro-symmetry property, i.e. with a skew-symmetric non-dimensional temperature field, ε_{12} will be machine zero. Conversely, flow fields that are symmetry breaking will exhibit a finite skewness. A plot showing the skewness metric was to be included only if the skewness metric was found to be non-zero.

In addition to the skewness metric, ε_{12}, three pressure differences ΔP_{14}, ΔP_{51} and ΔP_{35} were compulsory. The required pressure differences were defined as

$$\Delta P_{ij} = P_i - P_j \tag{19}$$

where i and j indicate the time-history points in Figure 1 and Table I used to compute the pressure difference.

3.3. Wall data

The wall Nusselt numbers were also compulsory and were requested at each wall as

$$Nu(t)|_{x=0,W} = \frac{1}{H}\int_0^H \left|\frac{\partial\theta}{\partial x}\right|_{x=0,W} \mathrm{d}y \tag{20}$$

3.4. Global data

An average velocity and vorticity metric were also requested as a part of the compulsory data. The average velocity metric was defined as

$$\hat{u}(t) = \sqrt{\frac{1}{2\mathscr{A}}\int_{\mathscr{A}} \mathbf{u}\cdot\mathbf{u}\,\mathrm{d}\mathscr{A}}, \tag{21}$$

where $\mathscr{A}$ is the area of the enclosure, $\mathscr{A} = W \times H$. Similarly, the measure of the average vorticity was defined as

$$\hat{\omega}(t) = \sqrt{\frac{1}{2\mathscr{A}}\int_{\mathscr{A}} \omega^2\,\mathrm{d}\mathscr{A}} \tag{22}$$

3.5. Methodology

A summary of the numerical method used to solve the thermal cavity problem was compulsory and was intended to provide a concise description of the following items:

- Spatial discretization method and a description of the grids used.
- Solution procedure, e.g. time-integration procedure, linear solvers, etc.
- Stopping criteria used for all iterative procedures.
- Description of the advective treatment—including any use of artificial viscosity, limiters, and blended first-/second-order methods.
- Description of any 'stabilizing' terms in the formulation or solution methodology, e.g., Galerkin least-squares (GLS) stabilization.

- An estimate of the order of accuracy of the method and, if possible, the accuracy of the submitted results.
- Any new or unique features of the method used to solve the differentially heated cavity problem.

3.6. Computational resources

A summary of the computational resources was also compulsory and intended to provide a concise description of the following items:

- Machine, e.g. Compaq, DEC, SGI, etc.,
- Clock rate in MegaHertz (MHz),
- Total memory MegaBytes (MBytes),
- peak FLOP (floating point operation) rate (MFLOPs) and/or the specFP95 rating—see: http://www.spec.org/osg/cpu95/,
- Number of processors used and the number of grid points per processor (degree of granularity) for parallel computations.
- CPU time (or wall clock time for parallel) used per grid point per time step (micro-seconds/point/step), and
- Memory used (per processor in parallel) (MBytes).

4. METHODS SUMMARY

This section summarizes the methods applied by the contributors to the 8:1 differentially heated cavity. There were 23 contributors to the special session at the MIT meeting who provided a total of 32 sets of solution data. Most of the contributors provided results computed on two or more grids. A complete list of the contributors may be found in the appendix—a subset of these contributions may be found in the papers included in this special issue.

The solution methods applied to the 8:1 cavity problem are presented in Table II and were predominantly finite element based with 22 of the 32 contributed solutions using some variant of the finite element method (FEM). There were also three spectral solutions (Nos. 18, 26 and 31), four finite-volume (FVM) (Nos. 5, 7, 8 and 27), two finite-difference solutions (FDM) (Nos. 16 and 25), and one based on Richardson extrapolation (No. 2). For a description of the finite element 'jargon', e.g. $Q_2 - Q_1$ element, refer to Reference [11].

In Table II, the mesh resolution is reported in terms of grid-points ($Nx \times Ny$) with the exception of the methods used by Paolucci (No. 18), Parolini (No. 26) and Le Quéré (No. 31). For Paolucci, in which a new set of divergence-free basis functions was used, the mesh resolution indicates the number of modes used in the x- and y-coordinate directions. For Parolini and Le Quéré, the mesh resolution indicates the number of modes used to represent each of the velocity and temperature fields. In subsequent comparisons, the total number of modes were counted as degrees of freedom in order to compute the computational cost on a per mode basis for each of the spectral contributions. The contributions by Bruneau (No. 16) and Johnston (No. 25) both used grids with uniform mesh spacing.

The majority of the contributed solutions were based on time-marching methods, and a majority of these solutions were obtained using primitive variables and segregated solution methods. Of the time-accurate, primitive variable solution methods, a total of 18 were

Table II. Methods summary for the contributed solutions.

No.	Corresponding author	Solution method (discretization; variables; element/time-integrator)	Mesh resolution
1	Comini-I	FEM; $u-P$; Q_1-Q_1; Crank–Nicolson/SIMPLE	21×101, 41×201 81×401
2	Comini-II	Richardson extrapolation based on results in No. 1	
3	Comini-III	FEM; $\psi-\omega$; Q_1; Crank–Nicolson	21×101, 41×201, 81×401
4	Comini-IV*	FEM; $\psi-\omega$; Q_1; Crank–Nicolson	81×401
5	Croce	FVM; $u-P$; collocated; Crank–Nicolson/SIMPLE	21×101, 41×201, 81×401
6	Westerberg	FEM; $u-P$; Q_2-Q_1; fully coupled/Newton/trapezoid rule	33×101, 49×161, 61×201
7	Ambrosini	FVM; $u-P$; staggered grid; segregated/SOR	21×101, 41×201, 61×301 81×401, 161×801
8	Kim	FVM; $u-P$; cell-centred; QUICK/3-step BDF/SIMPLE	81×401
9	Turek	FEM; $u-P$; non-conforming; fully coupled/multi-grid	129×705
10	Chan-I	FEM; $u-P$; Q_1-Q_0; FE+BTD/Crank–Nicolson/projection	81×401
11	Chan-II	FEM; $u-P$; Q_1-Q_1; FE+BTD/Crank–Nicolson/approximate projection	81×401
12	Chan-III	FEM; $u-P$; P_1-P_1; FE+BTD/Crank–Nicolson/approximate projection	81×401
13	Christon-I	FEM; $u-P$; Q_1-Q_0; one-point integration stabilized/FE+BTD	21×101, 41×201, 61×201 81×401
14	Christon-II	FEM; $u-P$; Q_1-Q_0; FE+BTD/Crank–Nicolson/projection	same as No. 13
15	Christon-III	FEM; $u-P$; Q_1-Q_0; fully implicit/predictor–corrector/projection	21×101
16	Bruneau	FDM; $u-P$; collocated, 3rd-order Murmann/centred/segregated	21×101, 41×201, 81×401, 161×801
17	Ingber	FEM; Vorticity; Q_1; Forward-Euler	81×401
18	Paolucci	Spectral Petrov–Galerkin; $u-P$; div-free basis functions	50×50, 50×70 (modes)
19	Pan	FEM; $u-P$; $P_1-iso-P_2/P_1$; wave-based advection/projection	17×129, 33×257, 65×512, 97×767

20	Christopher	FEM; $u-P$, $Q_2^{(8)}-Q_1$ Serendipity, fully coupled/pred.–corrector/Newton	$21\times101,\ 41\times201,\ 61\times201$
21	Davis	FEM; $u-P$, Q_2-Q_1, fractional-step/Backward-Euler, Crank–Nicolson	$23\times103,\ 43\times203,\ 83\times403$
22	Gresho-I	FEM; $u-P$, Q_1-Q_0, fully coupled/predictor–corrector/Newton	$27\times121,\ 53\times241,\ 105\times481$
23	Gresho-II	FEM; $u-P$, Q_2-P_{-1}, fully coupled/predictor–corrector/Newton	same as No. 22
24	Gresho-III	FEM; $u-P$, Q_2-Q_{-1}, fully coupled/predictor–corrector/Newton	same as No. 22
25	Johnston	FDM; $\psi-\omega$, 4th-order in space and time	$32\times256,\ 54\times512,\ 96\times768$
26	Parolini	Galerkin–Legendre Spectral; $u-P$, second-order BDF, projection	$21\times81,\ 31\times121,\ 41\times161$
27	Armfield	FVM; $u-P$, QUICK/semi-implicit/fractional-step	$35\times75,\ 69\times155,$ $141\times335,\ 293\times669$
28	Guo	FEM; $u-P$	41×121
29	Dunn	FEM; $u-P$; Q_1-Q_0; one-point integration stabilized/FE+BTD	$31\times101,\ 61\times201,\ 91\times301$
30	Matsumoto	FEM; $u-P$, P_1-P_1 w. bubble functions, semi-implicit projection	$21\times101,\ 41\times201$
31	Le Quéré	Chebyshev pseudo–spectral; $u-P$, Newton–Arnoldi stability, BDF2 with Adams–Bashforth convective for transient	$32\times120,\ 48\times180$
32	Salinger	GLS FEM; $u-P$; Q_1-Q_1, inexact Newton–Krylov stability	81×181

*Results submitted post-conference.

obtained using segregated methods, i.e. primarily SIMPLE or projection methods. Only seven contributed solutions were based on fully coupled primitive variable methods. The methods used by Christon (No. 15), Christopher (No. 20), Gresho and Sutton (Nos. 22–24), and Westerberg (No. 6) used second-order (trapezoidal rule) time-step control based on accuracy.

The contribution by Salinger *et al.* (No. 32), applied a Galerkin/least-squares finite element formulation with an inexact Newton–Krylov steady-state solver to estimate the first Hopf bifurcation. Similarly, Xin and Le Quéré, used a Chebyshev pseudo-spectral discretization in combination with a Newton Arnoldi–Krylov algorithm to map out four unstable branches in the 8:1 cavity for $3.0\times10^5 \leqslant Ra \leqslant 5.0\times10^5$. Parolini and Auteri used a Galerkin–Legendre second-order projection method to bound the first Hopf bifurcation in the range of $3.075\times10^5 \leqslant Ra_{\text{crit}} \leqslant 3.125\times10^5$. Bruneau and Saad also provided an estimate of Ra_{crit} by computing the first Lyapunov exponent for the linearized thermal convection system.

A total of five commercial flow solvers were applied to this problem: ADINA (No. 28), FIDAP (Nos. 22–24), Fluent (No. 8), LS-DYNA (Nos. 13–15), and PHOENICS (No. 20). Although not included in the subsequent comparison of solutions, Ambrosini *et al.* (No. 7) reported obtaining steady-state results using Fluent version 5.3 on the 41×201 grid. Although Christopher (No. 20) provided results computed using Nachos [12], he also reported an attempt to use PHOENICS v. 1.4 which failed due to the use of single precision variables and extreme mesh resolution required to obtain a time-dependent solution.

5. COMPARISON OF SOLUTIONS

This section presents a brief summary and comparison of the contributed solution data. For the purposes of comparison, only the contributed data computed with the most refined grid (and time-step) presented in Table II are used as this represents the most accurate results provided by each contributor at the MIT meeting. Please note that some authors have chosen to 'refine' their results in the papers included in this special issue relative to the results compiled at the MIT meeting which we present below.

5.1. Compulsory data

The compulsory data collected from all the contributors to the MIT special session are reported in Tables III and IV[‡]. In Table III, $\bar{u}_1$, $\bar{\theta}_1$, $\overline{Nu}$ and $\overline{\Delta P_{14}}$ are the time-averaged velocity, temperature, Nusselt number and pressure difference. The corresponding fluctuating velocity, temperature, Nusselt number and pressure difference are u'_1, θ'_1, Nu' and $\Delta P'_{14}$, respectively. The period, τ_θ, is the period associated with the temperature oscillation at time-history point-1. The number of time-steps per oscillation period are presented in Table V. Since the compulsory pressure differences, ΔP_{51} and ΔP_{35}, were not reported consistently for the MIT meeting, they have been omitted here.

The compulsory stream function, $\bar{\psi}$ and ψ', vorticity, $\bar{\omega}$ and ω' and the global velocity and vorticity metrics ($\bar{\hat{u}}$, $\hat{u}'$, and $\bar{\hat{\omega}}$, $\hat{\omega}'$, respectively) are reported in Table IV. Unfortunately,

[‡]The oscillation amplitudes and period reported in Tables III and IV for Johnston (No. 25) were collected prior to the First MIT meeting. This data was computed using a discrete Fourier transform, and corresponds to the results by Johnston and Krasny in Table III of their paper in this special issue.

Table III. Contributor-supplied data at time-history point-1.

No.	Corresponding author	$\bar{u}_1$	u_1'	$\bar{\theta}_1$	θ_1'	$\overline{Nu}$	Nu'	$\overline{\Delta P}_{14}$	$\Delta P_{14}'$	τ_θ
1	Comini-I	0.059800	0.074540	0.265440	0.056920	4.57850	0.009480	0.001965	0.026700	3.43250
2	Comini-II	0.058440	0.068560	0.265470	0.052860	4.57840	0.008778	0.001996	0.025280	3.42670
3	Comini-III	0.064800	0.095000	0.265700	0.072800	4.58500	0.011600			3.42000
4	Comini-IV	0.056567	0.053578	0.265189	0.042130	4.58239	0.007079			3.41250
5	Croce	0.060280	0.080280	0.266100	0.062480	4.57970	0.009460	0.003317	0.027560	3.44000
6	Westerberg	0.056630	0.058240	0.265500	0.045060	4.58700	0.007600	0.001810	0.021800	3.41000
7	Ambrosini	0.060800	0.080000	0.275000	0.050000			0.000896	0.027000	3.47000
8	Kim	0.054000	0.000480	0.265000	0.000260	9.14500	0.000050			5.05000
9	Turek	0.057200	0.056500	0.264700	0.044200	4.57910	0.007000	0.002000	0.020900	3.42200
10	Chan-I	0.061460	0.080580	0.264740	0.060960	4.57880	0.010460	0.001680	0.027940	3.50000
11	Chan-II	0.059290	0.083100	0.264820	0.063580	4.61200	0.010440	0.001830	0.027500	3.42700
12	Chan-III	0.059040	0.082500	0.264740	0.062980	4.61230	0.010380	0.001840	0.027340	3.42700
13	Christon-I	0.061120	0.050780	0.266300	0.039700	4.57900	0.006720	0.002328	0.018914	3.44700
14	Christon-II	0.065370	0.064320	0.267100	0.050040	4.56900	0.008410	0.003072	0.024120	3.47100
15	Christon-III	0.058670	0.055120	0.264140	0.042420	4.58022	0.007100			3.53617
16	Bruneau	0.059630	0.066160	0.268500	0.051380	4.58000	0.008450	0.001716	0.023760	3.40520
17	Ingber	0.064480	0.066100	0.268000	0.045520	4.47900	0.007208			3.40100
18	Paolucci	0.056453	0.051948	0.267803	0.040280	4.57942	0.007050			3.41271
19	Pan	0.057520	0.066120	0.266140	0.051080	4.57930	0.008358	0.001840	0.023940	3.42400
20	Christopher	0.055800	0.049300	0.265500	0.038600	4.58240	0.006500	0.005430	0.014380	3.42000
21	Davis	0.056300	0.054200	0.265500	0.042200	4.57960	0.007000	0.001800	0.020200	3.41200
22	Gresho-I	0.056930	0.055639	0.265145	0.043334	4.58210	0.007260	0.002343	0.020570	3.42790
23	Gresho-II	0.056650	0.055480	0.265470	0.043120	4.58250	0.007220	0.002190	0.020680	3.42590
24	Gresho-III	0.056493	0.055414	0.265722	0.043144	4.58210	0.007220	0.002030	0.020680	3.42590
25	Johnston	0.056160	0.054520	0.264700	0.042680	4.56700	0.007130	0.001375	0.020040	3.42200
26	Parolini	0.056700	0.053640	0.265460	0.044740	4.57950	0.007440	0.001840	0.021200	3.40680
27	Armfield	0.056380	0.053820	0.265600	0.041980	4.58000	0.006900	0.001855	0.020060	3.41250
28	Guo	0.056100	0.052940	0.265400	0.041340	4.57900	0.006890	0.002003	0.020032	3.42000
29	Dunn	0.057200	0.057500	0.266000	0.045000	4.58000	0.007520	0.001949	0.021500	3.44000
30	Matsumoto	0.060700	0.056432	0.244140	0.041240	4.67140	0.006358	0.000569	0.031780	3.34640
31	Le Quéré	0.056356	0.054828	0.265480	0.042740	4.57946	0.007100	0.001850	0.020380	3.41150

Table IV. Contributor-supplied vorticity and stream function at time-history point-1 and average velocity and vorticity.

No.	Corresponding author	$\bar{\psi}$	ψ'	$\bar{\omega}$	ω'	$\bar{\hat{u}}$	$\hat{u}'$	$\bar{\hat{\omega}}$	$\hat{\omega}'$
1	Comini-I	−7.120e-2	1.160e-2	−2.0208	1.8490	0.2411	3.800e-5	3.0122	4.200e-3
3	Comini-III	−7.170e-2	1.140e-2	−1.9914	1.9092	0.2425	4.000e-5	3.0162	4.000e-3
5	Croce	−7.077e-2	1.026e-2	−2.1480	1.6160	0.2373	5.700e-5	2.9830	4.640e-3
6	Westerberg	−7.357e-2	7.366e-3	−2.3370	1.1510	0.2396	3.590e-5	3.0170	3.353e-3
13	Christon-I	−7.405e-2	6.482e-3	−2.3200	0.9866	0.2398	3.500e-5	3.0160	3.160e-3
14	Christon-II	−7.313e-2	8.228e-3	−2.1950	1.2684	0.2388	7.200e-5	3.0060	3.780e-3
15	Christon-III	−7.394e-2	7.106e-3	−2.1213	0.9710	0.2403	7.000e-5		
16	Bruneau	−5.955e-2	7.895e-3	−2.1640	1.5830	0.2394	4.200e-5	2.7020	3.273e-3
18	Paolucci	−7.372e-2	6.990e-3	−2.3722	1.0750	0.2395	3.460e-5	3.0171	3.190e-3
19	Pan	−7.274e-2	8.387e-3	−2.2604	1.3257	0.2394	3.916e-5	3.0387	3.644e-3
20	Christopher	−7.370e-2	5.740e-3	−2.3708	0.9056	0.2393	3.100e-5	3.0340	2.900e-3
21	Davis					0.2395	3.300e-5		
22	Gresho-I	−7.450e-2	7.120e-3	−2.4144	1.0776	0.2397	3.460e-5	3.0075	3.220e-3
23	Gresho-II	−7.444e-2	7.080e-3	−2.4498	1.0816	0.2397	3.420e-5	3.0179	3.220e-3
24	Gresho-III	−7.439e-2	7.100e-3	−2.4455	1.0810	0.2397	3.400e-5	3.0179	3.220e-3
25	Johnston	−7.348e-2	6.856e-3	−2.3620	0.9940	0.2389	3.366e-5	3.0090	3.216e-3
26	Parolini	−7.359e-2	7.313e-3	−2.3548	1.1314	0.2396	3.467e-5	3.0169	3.300e-3
28	Guo	−7.385e-2	6.768e-3	−2.4334	1.0570	0.2395	3.278e-5	3.0172	3.116e-3
29	Dunn			−2.3600	1.1310	0.2400	4.610e-5	3.0200	3.310e-3
	Minimum	−7.450e-2	5.740e-3	−2.4498	0.9056	0.2373	3.100e-5	2.7020	3.000e-3
	Maximum	−5.955e-2	1.160e-2	−1.9914	1.9092	0.2425	7.200e-5	3.0387	4.640e-3
	Mean value	−7.249e-2	7.864e-3	−2.2845	1.2325	0.2397	4.093e-5	2.9998	3.488e-3
	Standard deviation	3.412e-3	1.675e-3	0.1439	0.3036	9.979e-4	1.216e-5	0.0774	4.266e-4

the stream function, vorticity, and global velocity and vorticity metrics were not reported consistently by all contributors at the MIT meeting. Therefore, these quantities are not included in subsequent comparisons. However, the minimum, maximum, mean and standard deviation for each quantity are reported in Table IV.

In order to account for variations in computational resources, algorithms and implementation details, a series of data that includes the computational 'grind-time', the number of time-steps per period, the specFP95 rating, and memory usage were requested as compulsory data. This data is presented in Table V. The grind-time is reported in milliseconds per node (grid-point) per time step with the concomitant number of time-steps per period of oscillation. As mentioned earlier, for the spectral methods, the number of modes were used rather than nodes in the calculation of the grind time. The contributions by Ingber (No. 17) and Dunn (No. 29) were performed in parallel, so the timing data for both are normalized on a total processor-time basis for comparison to the serial timing data provided by the other contributors.

5.2. *Data comparison*

As a baseline for comparison, we chose the contributed solution provided by Xin and Le Quéré as our 'truth' solution. This choice was based, in part, on the high convergence rate of the Chebyshev pseudo-spectral method which depends only on solution regularity, *and* in part on our 'special' request to them to provide a benchmark solution. In addition, the

Table V. Contributor-supplied performance data and computational resources used for the computations.

No.	Corresponding author	ms per node/step	Steps per period	Spec FP95		Memory (MBytes)	Machine
				Value	Basis		
1	Comini-I	0.54500	137.3	26.7	author	34.50	Olidata AMD K7 Athlon, 800 MHz, 512 MB
2	Comini-II	N/A					
3	Comini-III	0.57500	138.0	26.7	author	34.50	Olidata AMD K7 Athlon, 800 MHz, 512 MB
4	Comini-IV						No timing information given
5	Croce	0.12000	688.0	26.7	author	15.10	Olidata AMD K7 Athlon, 800 MHz, 512 MB
6	Westerberg	2.90000	16.0	20.0	estimate		SGI Octane 300 MHz R12000 processor
7	Ambrosini		270.0				No timing information given
8	Kim		120.0				Ultra Sparc 360 MHz processor
9	Turek	0.30000	38.4	83.0	estimate		Compaq ES40 667 MHz processor
10	Chan-I	0.90000	35.0	42.6	author	104.00	DEC Alpha
11	Chan-II		34.0				No timing information—Matlab code
12	Chan-III		34.0				No timing information—Matlab code
13	Christon-I	0.01211	1725.0	19.0	author	67.10	DEC Alpha 500 au, 500 MHz, 256 MB
14	Christon-I	0.10500	69.0	19.0	author	77.80	DEC Alpha 500 au, 500 MHz, 256 MB
15	Christon-III	0.10780	69.0	19.0	author	77.80	DEC Alpha 500 au, 500 MHz, 256 MB
16	Bruneau	0.00360	1200.0	82.7	author	12.00	Compaq ES40, 667 MHz, 2000 MB
17	Ingber	0.30336	1133.0	19.2	estimate		LosLobos, 32 processors, Intel PIII, 733 MHz, 1000 MB
18	Paolucci	0.60000	277.0	16.6	estimate	85.00	Ultra Sparc30, 296 MHz, 128 MB
19	Pan	0.01657	3424.0	50.9	estimate	9.97	IBM SP2, Power3-II, 375 Mhz, 4000 MB
20	Christopher	4.12570	137.0	11.8	estimate	210.00	Pentium III, 500 MHz, 256 MB
21	Davis	0.49000	341.0	53.9	author	130.00	COMPAQ XP1000, 500 MHz, 256 MB
22	Gresho-I	3.08000	25.0	52.3	author	26.78	HP J5000, 440 MHz, 2000 MB
23	Gresho-II	3.75000	25.0	52.3	author	33.53	HP J5000, 440 MHz, 2000 MB
24	Gresho-III	6.10000	25.0	52.3	author	33.73	HP J5000, 440 MHz, 2000 MB
25	Johnston	0.01230	438.0	19.5	author	11.41	DEC Alpha 500 au, 500 MHz, 1028 MB
26	Parolini	0.12210	3400.0	18.1	estimate	9.60	DEC Alpha 433 au, 433 MHz, 128 MB
27	Armfield	0.06840	2730.0	47.9	estimate	32.77	Compaq DS10, 466 MHz, 1000 MB
28	Guo	5.94000	34.8	25.0	estimate		IBM RS/6000
29	Dunn	0.09800	489.0	9.00	IBM		ASCI Blue, PowerPC 604e, 332 MHz
30	Matsumoto	0.30215	27.0	30.1	author		POWER 3 Super Chip
31	Le Quéré	0.09000	2024.0	52.0	estimate	36.00	SGI O2000, 300 MHz, 300 MB
32	Salinger	N/A	N/A				ASCI Red, 24 processors, Pentium II, 333 MHz, 256 MB

Table VI. Calculated percentage differences and ranking ($\mathcal{N}$) for each time-history value based on Xin and Le Quéré's (No. 31) results.

No.	Corresponding author	$\bar{\varepsilon}_{u_1}$	$\mathcal{N}$	ε'_{u_1}	$\mathcal{N}$	$\bar{\varepsilon}_{\theta_1}$	$\mathcal{N}$	ε'_{θ_1}	$\mathcal{N}$
1	Comini-I	6.1111	22	35.9524	23	−0.0151	7	33.1774	24
2	Comini-II	3.6979	16	25.0456	22	−0.0038	1	23.6781	23
3	Comini-III	14.9833	29	73.2691	29	0.0829	10	70.3323	29
4	Comini-IV	0.3739	6	2.2795	9	−0.1098	12	−1.4268	7
5	Croce	6.9629	23	46.4215	25	0.2335	16	46.1862	26
6	Westerberg	0.4862	8	6.2231	15	0.0075	3	5.4282	14
7	Ambrosini	7.8856	25	45.9108	24	3.5860	29	16.9864	19
8	Kim	−4.1806	18	−99.1245	30	−0.1808	14	−99.3917	30
9	Turek	1.4976	13	3.0495	11	−0.2938	21	3.4160	10
10	Chan-I	9.0567	27	46.9687	26	−0.2787	19	42.6299	25
11	Chan-II	5.2062	20	51.5649	28	−0.2486	17	48.7599	28
12	Chan-III	4.7626	19	50.4706	27	−0.2787	20	47.3561	27
13	Christon-I	8.4534	26	−7.3831	16	0.3089	23	−7.1128	17
14	Christon-II	15.9947	30	17.3123	18	0.6102	25	17.0800	20
15	Christon-III	4.1060	17	0.5326	1	−0.5047	24	−0.7487	2
16	Bruneau	5.8095	21	20.6683	21	1.1376	28	20.2153	22
17	Ingber	14.4155	28	20.5588	19	0.9492	27	6.5044	16
18	Paolucci	0.1721	3	5.2528	14	0.8750	26	−5.7557	15
19	Pan	2.0654	15	20.5953	20	0.2486	18	19.51334	21
20	Christopher	−0.9866	11	−10.2648	17	0.0075	4	−10.1545	18
21	Davis	−0.0994	2	1.1454	4	0.0075	5	−1.2635	5
22	Gresho-I	1.0185	12	1.4792	6	−0.1262	13	1.3903	6
23	Gresho-II	0.5217	9	1.1892	5	−0.0038	2	0.8891	3
24	Gresho-III	0.2427	4	1.0695	3	0.0912	11	0.9462	4
25	Johnston	−0.3478	5	−0.5618	2	−0.2938	22	−0.1404	1
26	Parolini	0.6104	10	−2.1668	8	−0.0075	6	4.6795	12
27	Armfield	0.0426	1	−1.8385	7	0.0452	9	−1.7782	8
28	Guo	−0.4543	7	−3.4435	12	−0.0301	8	−3.2756	9
29	Dunn	1.4976	14	4.8734	13	0.1959	15	5.2878	13
30	Matsumoto	7.70814	24	2.9255	10	−8.0383	30	−3.5096	11

senior corresponding author, Le Quéré, has extensive experience with thermally driven natural convection in enclosures—see for example References [2, 9, 10, 13]. However, it is arguable that other solutions may be as accurate as those provided by Le Quéré. For this reason, the raw data are provided in Tables III and IV, and the reader may process his own comparison based on these or other 'truth' solutions.

Table VI shows the calculated differences for the velocity and temperature at point-1 on a percentage basis for each entry relative to the 'truth' solution provided by Le Quéré (No. 31). Here, $\bar{\varepsilon}$ indicates the calculated percentage difference in the time-averaged values, and ε' indicates the calculated percentage difference in the peak-to-valley oscillation amplitude. Each tabulated result is ranked from the best with the smallest absolute value of the error, to the worst, with the largest absolute value of the error, as indicated by the rank $\mathcal{N}$. Most notable here is the fact that the mean temperature based on Richardson extrapolation (No. 2) was the most accurate. However, the other extrapolated results submitted by Comini *et al.* did not fare as well. The precise cause for this has not been explored at this time. The mean

Table VII. Calculated percentage differences and ranking ($\mathcal{N}$) for each time-history value based on Xin and Le Quéré's (No. 31) results.

No.	Corresponding author	$\bar{\varepsilon}_{Nu}$	$\mathcal{N}$	ε'_{Nu}	$\mathcal{N}$	$\bar{\varepsilon}_{\Delta P_{14}}$	$\mathcal{N}$	$\varepsilon'_{\Delta P_{14}}$	$\mathcal{N}$	$\varepsilon_{\tau_{\theta_1}}$	$\mathcal{N}$
1	Comini-I	−0.0210	14	33.5211	24	6.2162	9	31.0108	18	0.6156	21
2	Comini-II	−0.0231	15	23.6338	22	7.8919	11	24.0432	16	0.4456	17
3	Comini-III	0.1210	21	63.3803	28					0.2492	8
4	Comini-V	0.0640	18	−0.2986	2					0.0293	2
5	Croce	0.0052	5	33.2394	23	79.2973	23	35.2306	22	0.8354	22
6	Westerberg	0.1646	22	7.0423	16	−2.1622	6	6.9676	11	−0.0440	5
7	Ambrosini					−51.5676	20	32.4828	19	1.7148	25
8	Kim	99.6960	29	−99.2958	29					48.0287	30
9	Turek	−0.0079	6	−1.4084	5	8.1081	12	2.5515	8	0.3078	11
10	Chan-I	0.0144	12	47.3239	27	−9.1892	14	37.0952	23	2.5942	28
11	Chan-II	0.7106	25	47.0423	26	−1.0811	5	34.9362	21	0.4543	18
12	Chan-III	0.7171	26	46.1972	25	−0.5405	2	34.1511	20	0.4543	19
13	Christon-I	−0.0100	7	−5.3521	14	25.8378	18	−7.1933	12	1.0406	24
14	Christon-II	−0.2284	23	18.4507	20	66.0541	21	18.3513	15	1.7441	26
15	Christon-III	0.0166	13	0.0000	1					3.6544	29
16	Bruneau	0.0118	9	19.0141	21	−7.2432	10	16.5849	13	−0.1847	7
17	Ingber	−2.1937	28	1.5211	7					−0.3078	12
18	Paolucci	−0.0009	1	−0.7042	4					0.0355	4
19	Pan	−0.0035	4	17.7183	19	−0.5405	3	17.4681	14	0.3664	14
20	Christopher	0.0642	19	−9.8592	17	193.5135	24	−29.4406	17	0.2492	9
21	Davis	0.0031	3	−1.4084	6	−2.7027	7	−0.8832	1	0.0147	1
22	Gresho-I	0.0576	16	2.2535	10	26.6324	19	0.9323	2	0.4807	20
23	Gresho-II	0.0664	20	1.6901	8	18.3784	16	1.4720	3	0.4221	15
24	Gresho-III	0.0576	17	1.6901	9	9.7297	15	1.4720	4	0.4221	16
25	Johnston	−0.2721	24	0.4225	3	−25.6757	17	−1.6683	6	0.3078	13
26	Parolini	0.0009	2	4.7887	13	−0.5405	4	4.0236	9	−0.1378	6
27	Armfield	0.0118	10	−2.8169	11	0.2703	1	−1.5702	5	0.0293	3
28	Guo	−0.0100	8	−2.9577	12	8.2487	13	−1.7076	7	0.2492	10
29	Dunn	0.0118	11	5.9155	15	5.3514	8	5.4956	10	0.8354	23
30	Matsumoto	2.0077	27	−10.4507	18	−69.2432	22	55.9372	24	−1.9083	27

velocity result computed on a highly refined grid by Armfield (No. 27) was the most accurate, while the fourth-order FDM results provided by Johnston (No. 25) yielded the most accurate velocity and temperature oscillation amplitudes.

Table VII shows the calculated percentage differences in the average and amplitude of fluctuation for the Nusselt number, pressure difference, ΔP_{14} and period. Again, each result is ranked from the best to the worst as indicated by the rank $\mathcal{N}$, where the rank is based on the absolute value of the error. The most accurate time-averaged Nusselt number was reported by Paolucci (No. 1), while Christon (No. 15) reported the best oscillation amplitude. The best mean pressure difference was reported by Armfield (No. 27). The results provided by Davis (No. 21) were computed using the $Q_2 - Q_1$ element and yielded the most accurate peak-to-valley oscillation amplitude in the pressure difference, and the most accurate period of oscillation albeit with 341 time-steps per period.

The results presented in Tables VI and VII are naturally segregated into two primary groups based on the calculated differences. In the case of the mean velocity and velocity oscillation amplitude, there is a demarcation at 5% in each. In contrast, approximately half of the contributed solutions provided mean temperature results that fell in the category of $\bar{\varepsilon}_{\theta_1} \leqslant 0.2\%$, while the differences in the mean Nusselt number were below 1%. The errors in the temperature and Nusselt number oscillation amplitude also naturally segregated into two primary groups with about 12 of the contributions yielding $\varepsilon_{\theta_1'} \leqslant 5\%$ and $\varepsilon_{Nu'} \leqslant 5\%$. Perhaps not too surprisingly, the differences associated with the time-averaged pressure were not as good with a mean error of 26% and a maximum error of nearly 200% reported by Christopher (No. 20).

From the calculated and ranked differences, it is clear that the time-averaged velocity, temperature and Nusselt number were relatively 'easy' to calculate. This is reinforced by the mean differences for the time-averaged quantities shown in Tables VI and VII. In contrast, the oscillation amplitudes appear to reflect a larger component of error in all of the contributed solutions. This may be due to the fact that both spatial and temporal errors are reflected in the oscillation amplitudes. Overall, the largest errors in the oscillation amplitudes were for the results computed by Kim (No. 8) which failed to obtain a single-frequency time-dependent solution at $Ra = 3.4 \times 10^5$.

The raw data presented in Tables III–VII may be used to develop representative composite metrics based on the specific application of interest. We developed our own series of composite error metrics in order to perhaps obtain a somewhat more representative overall picture of the errors associated with the contributed solutions. These metrics are shown in Table VIII and consist of the average of the errors in the time-averaged velocity and temperature

$$\frac{|\bar{\varepsilon}_{u_1}| + |\bar{\varepsilon}_{\theta_1}|}{2} \tag{23}$$

the RMS (root mean square) of the time-averaged errors

$$\sqrt{\frac{\bar{\varepsilon}_{u_1}^2 + \bar{\varepsilon}_{\theta_1}^2}{2}} \tag{24}$$

the average of the errors in the velocity and temperature oscillation amplitude

$$\frac{|\varepsilon'_{u_1}| + |\varepsilon'_{\theta_1}|}{2} \tag{25}$$

and the RMS of the errors in the oscillation amplitude

$$\sqrt{\frac{[\varepsilon'_{u_1}]^2 + [\varepsilon'_{\theta_1}]^2}{2}} \tag{26}$$

The results in Table VIII are ranked from the smallest to the largest. We note that the rank order for the mean values and for the oscillation amplitudes are roughly independent of the specific norm used—in effect, a norm equivalence. Surprisingly, there is no clear distinction based on accuracy between the methods, i.e. finite element, finite volume, finite

Table VIII. Composite metrics and rank based on the velocity and temperature time-history data.

No.	Corresponding author	$(\lvert\bar{\varepsilon}_{u_1}\rvert + \lvert\bar{\varepsilon}_{\theta_1}\rvert)/2$		$\sqrt{(\bar{\varepsilon}_{u_1}^2 + \bar{\varepsilon}_{\theta_1}^2)/2}$		$(\lvert\varepsilon'_{u_1}\rvert + \lvert\varepsilon'_{\theta_1}\rvert)/2$		$\sqrt{([\varepsilon'_{u_1}]^2 + [\varepsilon'_{\theta_1}]^2)/2}$	
		Value (%)	$\mathcal{N}$	Value (%)	$\mathcal{N}$	Value (%)	$\mathcal{N}$	Value (%)	$\mathcal{N}$
1	Comini-I	3.0631	21	4.3212	22	34.5649	24	34.5927	23
2	Comini-II	1.8508	16	2.6148	16	24.3618	22	24.3714	22
3	Comini-III	7.5331	27	10.5950	29	71.8007	29	71.8157	29
4	Comini-IV	0.2418	4	0.2755	4	1.8531	8	1.9015	8
5	Croce	3.5982	23	4.9263	23	46.3039	26	46.3040	26
6	Westerberg	0.2469	6	0.3438	7	5.8256	15	5.8392	15
7	Ambrosini	5.7358	26	6.1254	25	31.4486	23	34.6146	24
8	Kim	2.1807	17	2.9589	18	99.2581	30	99.2582	30
9	Turek	0.8957	14	1.0792	14	3.2328	10	3.2380	10
10	Chan-I	4.6677	25	6.4071	26	44.7993	25	44.8518	25
11	Chan-II	2.7274	20	3.6855	20	50.1624	28	50.1820	28
12	Chan-III	2.5207	19	3.3734	19	48.9133	27	48.9381	27
13	Christon-I	4.3811	24	5.9814	24	7.2479	16	7.2492	16
14	Christon-II	8.3025	30	11.3182	30	17.1962	19	17.1966	19
15	Christon-III	2.3054	18	2.9253	17	0.6406	2	0.6497	2
16	Bruneau	3.4735	22	4.1859	21	20.4418	21	20.4430	21
17	Ingber	7.6824	28	10.2154	28	13.5316	18	15.2475	18
18	Paolucci	0.5236	11	0.6306	10	5.5043	14	5.5100	14
19	Pan	1.1570	15	1.4710	15	20.0543	20	20.0616	20
20	Christopher	0.4971	10	0.6976	11	10.2096	17	10.2098	17
21	Davis	0.0535	2	0.0705	2	1.2044	5	1.2059	5
22	Gresho-I	0.5724	12	0.7257	12	1.4347	6	1.4354	6
23	Gresho-II	0.2627	7	0.3689	8	1.0391	4	1.0499	4
24	Gresho-III	0.1669	3	0.1833	3	1.0079	3	1.0097	3
25	Johnston	0.3208	9	0.3219	6	0.3511	1	0.4094	1
26	Parolini	0.3090	8	0.4317	9	3.4231	12	3.6464	12
27	Armfield	0.0439	1	0.0439	1	1.8083	7	1.8086	7
28	Guo	0.2422	5	0.3219	5	3.3596	11	3.3606	11
29	Dunn	0.8467	13	1.0680	13	5.0806	13	5.0848	13
30	Matsumoto	7.8732	29	7.8749	27	3.2176	9	3.2308	9

difference, fully coupled or segregated. Again, the computations by Armfield (No. 27) have the smallest errors in the time-averaged velocity–temperature metrics, while the contribution by Johnston (No. 25) has the smallest errors in the velocity–temperature oscillation amplitude metrics.

A summary of the minimum and maximum absolute value in the computed errors presented in Table IX along with the mean value and standard deviation for each. Here, the most accurate and least accurate results in an absolute sense are reported without regard for the computational cost. Again, the fact that the mean values of temperature and velocity were relatively easy to compute while the pressure and fluctuating components were more prone to errors is reflected in the mean error values.

Three overall accuracy metrics were constructed and the results for each contributor are shown in 'rank-order' in Table X. These metrics reflect only the accuracy of the contributed

Table IX. Summary of minimum and maximum absolute values of error metrics for all and performance metrics for all contributed solutions.

	Minimum			Maximum				
Metric	No.	Corresponding author	Metric value	No.	Corresponding author	Metric value	Mean value	Standard deviation
$\bar{\varepsilon}_{u_1}$	27	Armfield	0.0426	14	Christon-II	15.9947	4.3326	4.6668
ε'_{u_1}	15	Christon-III	0.5326	8	Kim	99.1245	21.0003	24.8253
$\bar{\varepsilon}_{\theta_1}$	2	Comini-II	0.0038	30	Matsumoto	8.0383	0.6267	1.5275
ε'_{θ_1}	25	Johnston	0.1404	8	Kim	99.3917	18.3005	23.6178
$\frac{1}{2}(\lvert\bar{\varepsilon}_{u_1}\rvert + \lvert\bar{\varepsilon}_{\theta_1}\rvert)$	27	Armfield	0.0439	14	Christon-II	8.3025	2.4158	2.6223
$\sqrt{\frac{1}{2}([\bar{\varepsilon}_{u_1}]^2 + [\bar{\varepsilon}_{\theta_1}]^2)}$	27	Armfield	0.0439	14	Christon-II	11.3182	3.1041	3.3662
$\frac{1}{2}(\lvert\varepsilon'_{u_1}\rvert + \lvert\varepsilon'_{\theta_1}\rvert)$	25	Johnston	0.3511	8	Kim	99.2581	19.3128	23.9843
$\sqrt{\frac{1}{2}([\varepsilon'_{u_1}]^2 + [\varepsilon'_{\theta_1}]^2)}$	25	Johnston	0.4094	8	Kim	99.2582	19.4938	24.0288
$\bar{\varepsilon}_{\Delta P_{14}}$	27	Armfield	0.2703	20	Christopher	193.5135	26.0840	41.8860
$\varepsilon'_{\Delta P_{14}}$	21	Davis	0.8832	30	Matsumoto	55.9372	16.7779	15.7097
$\bar{\varepsilon}_{Nu}$	18	Paolucci	0.0009	8	Kim	99.6960	3.6749	18.1542
ε'_{Nu}	15	Christon-III	0.0000	8	Kim	99.2958	17.5654	23.2644
$\varepsilon_{\tau_{\theta_1}}$	21	Davis	0.0147	8	Kim	48.0287	2.2721	8.5368
η_{AT}	25	Johnston	1.0000	17	Ingber	2010.1368	115.0350	388.2903
η_{MCPU}	16	Bruneau	1.0000	20	Christopher	2289.6680	190.4220	503.1299

results regardless of the grid resolution or computational cost. The first metric

$$E_1 = \frac{(\bar{\varepsilon}_{Nu} + \bar{\varepsilon}_{u_1} + \bar{\varepsilon}_{\theta_1})}{3} \tag{27}$$

consists of an average of mean differences in the Nusselt number, x-velocity and temperature. The second overall metric

$$E_2 = \frac{(\varepsilon_{\tau_{\theta_1}} + \varepsilon'_{Nu} + \varepsilon'_{u_1} + \varepsilon'_{\theta_1})}{4} \tag{28}$$

is the average of the period and amplitude errors. The third overall metric, E_3, is the average of the errors computed in the period, mean velocity, temperature and Nusselt number, and the corresponding error in the oscillation amplitudes

$$E_3 = \frac{(\bar{\varepsilon}_{Nu} + \bar{\varepsilon}_{u_1} + \bar{\varepsilon}_{\theta_1} + \varepsilon_{\tau_{\theta_1}} + \varepsilon'_{Nu} + \varepsilon'_{u_1} + \varepsilon'_{\theta_1})}{7} \tag{29}$$

The inclusion of the oscillation period error in metrics E_2 and E_3 results in a slightly different ranking as well as larger errors relative to E_1. However, there is again essentially a 'norm equivalence' between the overall metrics 2 and 3. There is an overall segregation of the contributed solutions into two primary groups—roughly speaking, it is those in the top 15 and those in the bottom 15. In the case of the E_1 metric, the bottom 14 results correspond to $E_1 \geqslant 1.0\%$, and for E_3, the bottom 14 are identified by $E_3 \geqslant 5.0\%$. In terms of E_2,

Table X. Overall rankings based on error metrics presented in rank-order for metrics E_1–E_3.

	Overall metric E_1			Overall metric E_2			Overall metric E_3		
Rank Order $\mathcal{N}$	No.	Corresponding author	Metric value	No.	Corresponding author	Metric value	No.	Corresponding author	Metric value
1	27	Armfield	0.0332	25	Johnston	0.3581	25	Johnston	0.3352
2	21	Davis	0.0367	21	Davis	0.9580	21	Davis	0.5631
3	24	Gresho-III	0.1305	4	Comini-IV	1.0085	24	Gresho-III	0.6456
4	28	Guo	0.1648	24	Gresho-III	1.0320	4	Comini-IV	0.6545
5	4	Comini-IV	0.1826	23	Gresho-II	1.0476	23	Gresho-II	0.6832
6	23	Gresho-II	0.1973	15	Christon-III	1.2339	27	Armfield	0.9375
7	26	Parolini	0.2063	15	Gresho-I	1.4009	22	Gresho-I	0.9723
8	6	Westerberg	0.2195	27	Armfield	1.6157	15	Christon-III	1.3662
9	25	Johnston	0.3046	9	Turek	2.0454	9	Turek	1.4259
10	18	Paolucci	0.3493	28	Guo	2.4815	28	Guo	1.4886
11	20	Christopher	0.3528	18	Paolucci	2.9371	26	Parolini	1.7702
12	22	Gresho-I	0.4008	26	Parolini	2.9432	18	Paolucci	1.8280
13	29	Dunn	0.5684	29	Dunn	4.2280	29	Dunn	2.6596
14	9	Turek	0.5998	6	Westerberg	4.6844	6	Westerberg	2.7708
15	19	Pan	0.7725	30	Matsumoto	4.6985	13	Christon-I	4.2373
16	2	Comini-II	1.2416	13	Christon-I	5.2221	20	Christopher	4.5123
17	15	Christon-III	1.5425	17	Ingber	7.2231	30	Matsumoto	5.2212
18	12	Chan-III	1.9195	20	Christopher	7.6319	17	Ingber	6.6358
19	1	Comini-I	2.0491	14	Christon-II	13.6468	19	Pan	8.6444
20	11	Chan-II	2.0551	19	Pan	14.5483	16	Bruneau	9.5773
21	16	Bruneau	2.3196	16	Bruneau	15.0206	14	Christon-II	10.2029
22	5	Croce	2.4005	2	Comini-II	18.2008	2	Comini-II	10.9325
23	13	Christon-I	2.9241	7	Ambrosini	21.5374	7	Ambrosini	15.2167
24	10	Chan-I	3.1166	1	Comini-I	25.8166	1	Comini-I	15.6305
25	3	Comini-III	5.0624	5	Croce	31.6707	5	Croce	19.1263
26	14	Christon-II	5.6111	10	Chan-I	34.8792	10	Chan-I	21.2666
27	7	Ambrosini	5.7358	12	Chan-III	36.1196	12	Chan-III	21.4624
28	17	Ingber	5.8528	11	Chan-II	36.9554	11	Chan-II	21.9981
29	30	Matsumoto	5.9180	3	Comini-III	51.8077	3	Comini-III	31.7740
30	8	Kim	34.6858	8	Kim	86.4602	8	Kim	64.2712

the demarcation point is $E_2 \geqslant 5.0\%$ with 14 of the contributed solutions falling in this category.

The results in Tables VI–X provide an indication of best accuracy, but they do not reflect the computational cost required to obtain the solution. In order to account for differences in algorithms, computing resources, and implementation, a normalized algorithm timing and a memory footprint metric were developed based on the contributor-supplied performance data. The normalized algorithm timing is based on the data reported in Table V and is defined as

$$\eta_{\mathrm{AT}} = \left[\frac{\mathrm{msec}}{\mathrm{node}\cdot\mathrm{step}} \cdot \frac{\mathrm{steps}}{\mathrm{period}}\right] \cdot \mathrm{specFP95} \tag{30}$$

Table XI. Normalized algorithm timing and memory-CPU metrics.

No.	Corresponding author	η_{AT}	$\mathcal{N}$	η_{MCPU}	$\mathcal{N}$
1	Comini-I	19.02	11	49.80	9
3	Comini-III	20.17	12	52.81	10
5	Croce	20.98	13	24.05	6
6	Westerberg	8.83	7		
9	Turek	9.10	8		
10	Chan-I	12.77	9	63.19	12
13	Christon-I	3.78	6	27.04	7
14	Christon-II	1.31	2	10.87	3
15	Christon-III	1.35	3	11.16	5
16	Bruneau	3.40	5	1.00	1
17	Ingber	2010.14	25		
18	Paolucci	13.13	10	136.26	17
19	Pan	27.49	14	10.91	4
20	Christopher	63.43	18	2289.67	19
21	Davis	85.73	22	419.01	18
22	Gresho-I	38.33	15	39.78	8
23	Gresho-II	46.67	16	60.64	11
24	Gresho-III	75.92	20	99.23	14
25	Johnston	1.00	1	1.19	2
26	Parolini	71.53	19	76.88	13
27	Armfield	85.14	21	118.04	15
28	Guo	49.19	17		
29	Dunn	114.95	24		
30	Matsumoto	2.34	4		
31	LeQuéré	90.17	23	126.50	16

The normalized memory-CPU metric is defined as

$$\eta_{MCPU} = \left[\frac{\text{msec}}{\text{node} \cdot \text{step}} \cdot \frac{\text{steps}}{\text{period}}\right] \cdot \text{Memory} \tag{31}$$

where Memory is reported in MegaBytes (MB).

Both of the normalized performance metrics are scaled in a relative sense so that the minimum η_{AT} and minimum η_{MCPU} are unity. The normalized performance metrics are presented in Table XI along with a ranking from best to worst in terms of the normalized CPU and memory-CPU metrics. It is not surprising that the segregated methods tend to have smaller normalized CPU and memory-CPU metrics. It is worth nothing that the unstructured-grid finite element methods reported by Christon (Nos. 14 and 15) are ranked a close second (semi-implicit) and third (fully implicit) to the fourth-order finite-difference method of Johnston's finite-difference method in terms of the normalized algorithm timing.

The most efficient and least efficient computations are reflected in a relative sense in Table XI by the normalized memory-CPU metric, η_{MCPU}, and the normalized algorithm timing, η_{AT} values. The fourth-order stream function—vorticity method of Johnston (No. 25) has the best grind-time, while the comparable stream function—vorticity finite element solution of Ingber (No. 17) was about 2000 times more expensive to compute. The finite difference method of Bruneau (No. 16) had the smallest memory-CPU metric, while the fully coupled

finite element solution provided by Christopher (No. 20) required a memory-CPU integral nearly 2300 times greater.

In order to account for accuracy and the computational cost, three additional overall metrics were constructed using the normalized algorithm timing and the grid resolution. These metrics are shown in Table XII for each contributor and consist of a resolution weighted metric

$$E_4 = E_3 \cdot (\text{No. of nodes}) \tag{32}$$

the overall error metric, E_3, weighted by the normalized algorithm timing

$$E_5 = E_3 \cdot \eta_{\text{AT}} \tag{33}$$

and the overall error metric, E_3, weighted by the normalized algorithm timing and resolution,

$$E_6 = E_3 \cdot \eta_{\text{AT}} \cdot (\text{No. of nodes}) \tag{34}$$

Again, the No. of nodes was adjusted to reflect the actual computational cost of the spectral methods submitted by Paolucci (No. 18), Parolini (No. 26), and Le Qéré (No. 31) based on the actual degrees of freedom computed.

The overall metrics, E_4–E_6 shown in Table XII are presented in 'rank-order' according to the ranking, $\mathcal{N}$, for each metric. These metrics reflect both the accuracy and the computational cost required to achieve the solution. Surprisingly, the fully implicit second-order FEM projection method used by Christon (No. 15) appears to provide the best overall balance between computational cost and accuracy followed closely by the fourth-order method of Johnston (No. 25) and the Petrov–Galerkin method of Paolucci (No. 18). Matsumoto (No. 30) used $P_1 - P_1$ triangular elements to achieve good algorithm performance as reflected by the ranking in metrics E_5 and E_6. The only methods using higher-order finite elements that are ranked at least once in the top five are those used by Davis (No. 21) for the E_4 metric and Westerberg (No. 6) for the E_6 metric. Interestingly, *both* were performed using a relatively *un*popular finite element: $Q_2 - Q_1$; see Reference [11]. Also interesting is the difference in the number of time-steps per oscillation period used: whereas Davis used 341 steps per period, Westerberg, who was not far behind in the overall rankings, used only 16 steps per period (see Table V). Otherwise, there is no clear distinction between the overall performance of the finite element, finite difference and finite volume methods applied to the thermally driven cavity problem.

5.3. The critical Rayleigh number

Several contributors provided estimates of the critical Rayleigh number, above which the flow is unsteady. First, the contribution by Parolini and Auteri (No. 26) used their Galerkin–Legendre projection method to bound the first Hopf bifurcation in the range of $3.075 \times 10^5 \leqslant Ra_{\text{crit}} \leqslant 3.125 \times 10^5$. Bruneau and Saad (No. 16) computed the first Lyapunov exponent and estimated the critical Rayleigh number as $Ra_{\text{crit}} = 2.9 \times 10^5$. Using a grid resolution of 181 $\times$ 801, they obtained unsteady results at $Ra = 3.0 \times 10^5$ with a oscillation period of 3.7. Finally, both Salinger (No. 32) and Le Quéré (No. 31) computed the first and second bifurcation points. Their computation of the first and second critical Rayleigh numbers are shown in Table XIII with the period of oscillation.

Table XII. Overall rankings based on error metrics, weighted by the computational performance factors, and presented in rank-order.

Rank order $\mathcal{N}$	Overall metric E_4			Overall metric E_5			Overall metric E_6		
	No.	Corresponding author	Metric value	No.	Corresponding author	Metric value	No.	Corresponding author	Metric value
1	15	Christon-III	1.00	25	Johnston	1.00	15	Christon-III	1.00
2	18	Paolucci	3.06	15	Christon-III	3.95	25	Johnston	8.79
3	28	Guo	3.53	30	Matsumoto	36.41	18	Paolucci	29.90
4	26	Parolini	5.59	9	Turek	38.72	30	Matsumoto	35.79
5	21	Davis	9.01	14	Christon-II	39.89	6	Westerberg	106.79
6	25	Johnston	11.82	13	Christon-I	47.76	28	Guo	129.27
7	24	Gresho-III	15.61	18	Paolucci	71.62	14	Christon-II	154.52
8	6	Westerberg	16.26	6	Westerberg	73.03	13	Christon-I	185.03
9	23	Gresho-II	16.51	23	Gresho-II	95.14	26	Parolini	297.41
10	20	Christopher	17.80	16	Bruneau	97.18	9	Turek	419.99
11	30	Matsumoto	20.59	22	Gresho-I	111.20	23	Gresho-II	573.06
12	22	Gresho-I	23.51	21	Davis	144.04	21	Davis	574.62
13	17	Ingber	26.18	24	Gresho-III	146.25	22	Gresho-I	669.85
14	29	Dunn	34.87	28	Guo	218.49	20	Christopher	839.38
15	9	Turek	62.08	27	Armfield	238.15	24	Gresho-III	880.94
16	13	Christon-I	65.89	26	Parolini	377.77	16	Bruneau	1494.65
17	27	Armfield	91.91	19	Pan	709.12	29	Dunn	2979.98
18	14	Christon-II	158.64	10	Chan-I	810.49	10	Chan-I	3139.77
19	7	Ambrosini	236.60	20	Christopher	854.00	1	Comini-I	3435.82
20	1	Comini-I	243.04	1	Comini-I	886.91	5	Croce	4638.65
21	5	Croce	297.39	29	Dunn	912.19	27	Armfield	5817.23
22	19	Pan	307.87	5	Croce	1197.41	19	Pan	6292.23
23	10	Chan-I	330.67	3	Comini-III	1911.87	3	Comini-III	7406.43
24	12	Chan-III	333.72	17	Ingber	39798.05	17	Ingber	39116.70
25	11	Chan-II	342.04						
26	3	Comini-III	494.05						
27	16	Bruneau	591.25						
28	8	Kim	999.35						

Table XIII. Critical Rayleigh numbers for the first and second bifurcation points.

		First		Second		
Author	No.	Ra_{crit}	Period	Ra_{crit}	Period	Mesh resolution
Le Quéré	31	306191.6	3.6763464	311169.8	3.4242277	40×140
Salinger	32	306450	3.6759	311480	N/A	257×689

6. SUMMARY AND CONCLUSIONS

The primary objectives for this endeavor were to determine the most accurate estimate of the critical Rayleigh number above which the flow is unsteady, identify the correct, i.e. best time-dependent benchmark solution for the 8:1 differentially heated cavity, and identify those methods that can reliably provide these results. The first critical Rayleigh number provided in the 'truth' solution by Xin and Le Quéré marks the transition from steady to a time-dependent flow at $Ra_{crit} = 3.0619 \times 10^5$, while the second critical Rayleigh number marks the transition to a time-dependent skew-symmetric flow at $Ra_{crit} = 3.1117 \times 10^5$. This has been further verified by the GLS/FEM results provided by Salinger *et al.* (No. 32)—albeit using a factor of 32 more grid resolution.

Unfortunately, the identification of the 'best' time-dependent solution was less clear cut. As mentioned earlier, our choice for a 'truth' solution was that of Xin and Le Quéré, although it is clear that other equivalent baseline solutions could be used. While it was initially thought that there would be a clear distinction between fully coupled and segregated solution methods, when the cost of obtaining solutions is accounted for, there seems to be no such clear distinction. However, if we were tasked with selecting an 'overall' 'best' contributed solution based on accuracy (and, thankfully, we were not!), it would probably be that of Davis and Bänsch (No. 21). Their rankings were consistently high for both the computed errors (Tables VI and VII) and in the composite metrics in Table VIII. Their average ranking for these error metrics was about 3.7, and they were ranked 2nd in all of the overall accuracy metrics ($E_1 - E_3$) in Table X.

In contrast to the results found by de Vahl Davis [14], there seems to be no clear indicator that the FEM flow solvers are more accurate than their FDM or FVM counterparts. This is perhaps difficult to assess because the contributed solutions were predominantly finite element based while the finite difference and finite volume method were somewhat under-represented. However, the answer to the question as to which methods can reliably deliver accurate solutions to the 8:1 thermally driven cavity is that there is more than one. It was encouraging, if somewhat surprising, that most of the results were relatively consistent with only a few 'poor' results. While most contributors did not demonstrate grid or time-step convergence, most of the results were relatively consistent with only a few extremely poor results. Those methods that achieved calculated differences of less than 5% in the oscillation amplitudes for the velocity, temperature and Nusselt number relative to Le Quéré's solution are all reasonable choices for attacking this class of flow problem, and with appropriate care given to details will yield acceptable results with a variety of methods.

As to the use of higher-order finite element methods, the low-order $Q_1 - Q_0$ element did very well with respect to higher-order elements. (This element provides a spatial discretization that

is the closest to many popular finite-volume methods.) In addition, the Q_2-Q_{-1} element fared slightly better than the Q_2-P_{-1}. Most surprising, though, were the good results obtained with the 'old' Taylor–Hood element, Q_2-Q_1. However, in terms of the combined accuracy-cost metrics, the higher-order elements did not perform better than their low-order counterparts.

Finally, given the rather wide range in the grid resolution (about a factor of 7), and the very large range of time step sizes (about a factor of 200), it is problematic to directly compare different contributions to the 'truth' solution—particularly since a convergent method will deliver a more accurate solution on a refined grid. In order to account for this possibility, our composite error metrics were constructed based on the mesh resolution and computational resources required to deliver the solutions (see E_4-E_6 in Table XII). Although these metrics attempt to place the contributed solutions on an equal footing, it is up to the CFD practitioner to decide the appropriate balance between computational efficiency and accuracy.

APPENDIX

The following list contains the names and addresses of all contributors numbered in the order that their contributions were received.

1. G. Comini, M. Manzan, C. Nonino and O. Saro, Dipartimento di Energetica e Macchine, Universita di Udine, Via delle Science 208, 33100, Udine, Italy.
2. G. Croce and M. Favero, Dipartimento di Energetica e Macchine, Universita di Udine, Via delle Science 208, 33100, Udine, Italy.
3. K. Westerberg (deceased), Lawrence Livermore National Laboratory, L-130, P.O. Box 808, Livermore, California, 94550, U.S.A.
4. W. Ambrosini, J. C. Ferreri and N. Forgione, Riceratore, Universita' degli Studi di Pisa, Facolta' di Ingegneria, Dipartmento di Ingegneria Meccanica, Nulceare e della Produzione, Via Diotisalvi, 2, 56126, Pisa, Italy.
5. S.-E. Kim and D. Choudhury, Fluent Inc., Lebanon, New Hampshire, 03766, U.S.A.
6. S. Turek, Institute for Applied Mathematics and Numerics, LS III, University of Dortmund, Vogelpothsweg 87, D-44227 Dortnumd, Germany.
7. S. Chan and D. Stevens, Lawrence Livermore National Laboratory, L-130, P.O. Box 808, Livermore, California, 94550, U.S.A.
8. M. Christon, Sandia National Laboratories, M/S 0819, P.O. 5800, Albuquerque, New Mexico, 87185-0819, U.S.A.
9. C.-H. Bruneau and M. Saad, Mathematiques Appliquees de Bordeau, Universite Bordeau 1, 351, Cour de la Liberation 33405, Talence, France.
10. M. Ingber, Mechanical Engineering Department, University of New Mexico, Albuquerque, New Mexico 87131, U.S.A.
11. S. A. Suslov and S. Paolucci, Department of Aerospace and Mechanical Engineering, University of Notre Dame, Notre Dame, Indiana, 46556, U.S.A.
12. T.-W. Pan and R. Glowinski, Department of Mathematics, University of Houston, Houston, Texas 77204, U.S.A.
13. D. M. Christopher, Thermal Engineering Department, Tsinghua University, Beijing, 100084, China.

14. D. Davis and E. Bänsch, Weierstrass Institute for Applied Analysis and Stochastics, Mohrenstrasse 39, D-10117 Berlin, Germany.
15. P. M. Gresho and S. B. Sutton, Lawrence Livermore National Laboratory, L-130, P.O. Box 808, Livermore, California, 94550, U.S.A.
16. H. Johnston and R. Krasny, Department of Mathematics, University of Michigan, Ann Arbor, Michigan, 48109, U.S.A.
17. F. Auteri and N. Parolini, Dipartimentio di Ingegneria Aerospaziale, Politecnico di Milano, v. La Masa 34, 20158 Milano, Italy.
18. S. Armfield, Department of Mechanical Engineering, Sydney University, Sydney 2006, Australia.
19. Y. Guo and K.-J. Bathe, ADINA R&D, Inc., 71 Elton Avenue, Watertown, Massachussets 02472, U.S.A.
20. T. Dunn and R. McCallen, Lawrence Livermore National Laboratory, L-228, P. O. Box, 808, Livermore, California 94450, U.S.A.
21. S. Matsumoto, Department of Civil Engineering, Chuo University, Kasuga 1-13-27, Bunkyo-ku, Tokyo 112-8551, Japan.
22. S. Xin and P. Le Quéré, LIMSI-CNRS, BP 133, 91403 Orsay Cedex, France.
23. A. Salinger, R. B. Lehoucq, R. P. Pawlowski and J. N. Shadid, Sandia National Laboratories, M/S 1111, P.O. Box 5800, Albuquerque, New Mexico 87185-1111, U.S.A.

ACKNOWLEDGEMENTS

We would like to express our sincere thanks to all those that contributed to the special session at the First MIT meeting and to this special issue. We would also like to extend our deepest appreciation to Prof K.J. Bathe for embracing our proposal for a special session and making it possible for us to dedicate an extended series of technical sessions to the 8:1 thermally driven cavity at the First MIT Meeting on Computational Fluid and Solid Mechanics.

REFERENCES

1. Winters KH. Hopf bifurcation in the double-glazing problem with conducting boundary. *Journal of Heat Transfer* 1988; **109**:894–898.
2. Le Quéré P. Onset of unsteadiness, routes to chaos and simulations of chaotic flows in cavities heated from the side: a review of present status. In *Proceedings of the Tenth International Heat Transfer Conference, Brighton, UK* Hewitt GF (ed.). Rugby, Warwickshire, UK: Institution of Chemical Engineers 1994; 281–296.
3. Gill AE. The boundary-layer regime for convection in a rectangular cavity. *Journal of Fluid Mechanics* 1966; **26**:515–536.
4. Gadoin E, Le Quéré P, Caube O. A general methodology for investigating flow instabilities in complex geometries: application to natural convection in enclosure. *International Journal for Numerical Methods in Fluids* 2001; **379**:175–208.
5. Xin S, Le Quéré P. *Personal communication*, July 2000.
6. Gresho PM, Chan ST, Lee RL, Upson CD. A modified finite element method for solving the time-dependent, incompressible Navier–Strokes equations. Part 1: Theory. *International Journal for Numerical Methods in Fluids* 1984; **4**:557–598.
7. Bathe KJ (ed.). *First MIT Meeting on Computational Solid and Fluid Mechanics*, vols. 1 and 2. MIT Elsevier: New York, June 2001.
8. De Vahl Davis G. Finite difference methods for natural and mixed convection in enclosures. *In Proceedings of the 8th International Heat Transfer Conference*, ASME, August 1986; 101–109.
9. Le Quéré P, De Roquefort TA. Transition to unsteady natural convection of air in vertical differentially heated cavities influence of thermal boundary conditions on the horizontal walls. In *Proceedings of International Heat Transfer Conference* ASME, August 1986.
10. Le Quéré P, Behnia M. From onset of unsteadiness to chaos in a differentially heated cavity. *Journal of Fluid Mechanics* 1998; **359**:81–107.

11. Gresho PM, Sani RL, Engelman MS. *Incompressible Flow and the Finite Element Method*, vol. 2, *Isothermal Laminar Flow.* Wiley: Chichester, England, 2000.
12. Gartling DK. Finite element computer program for incompressible flow problems. Part 1—theoretical background. *Technical report*, Sandia National Laboratories, April 1987.
13. Le Quéré P. A note on multiple and unsteady solutions in two-dimensional convection in a tall cavity. *Journal of Heat Transfer* 1990; **112**:965–974.
14. De Vahl Davis G, Jones IP. Natural convection in a square cavity: a comparison exercise. *International Journal for Numerical Methods in Fluids* 1983; **3**:227–248.

